

Detrimental impact of Na upon Rb post deposition treatments of Cu(In,Ga)Se₂ absorber layers

Jessica de Wild^{A,B,C,}, Gizem Birant^{A,B,C}, Raghavendran Thiruvallur Eachambadi^D, Thierry Kohl^{A,B,C}, Dilara G. Buldu^{A,B,C}, Guy Brammertz^{A,B,C}, Jean V. Manca^D, Marc Meuris^{A,B,C}, Jef Poortmans^{A,C,E,F}, Bart Vermang^{A,B,C}*

Dr. J. de Wild, G. Birant, T. Kohl, D.G. Buldu, Dr. G. Brammertz, Dr. M. Meuris, Prof. J. Poortmans, Prof. B. Vermang

A. Institute for Material Research (IMO), Hasselt University (partner in Solliance),
Wetenschapspark 1, 3590 Diepenbeek, Belgium

Email: Jessica.deWild@imec.be

Dr. J. de Wild, G. Birant, T. Kohl, D.G. Buldu, Dr. G. Brammertz, Dr. M. Meuris, Prof. B. Vermang

B. U Hasselt - IMOMECE, imec (partner in Solliance), Wetenschapspark 1, 3590 Diepenbeek,
Belgium

Dr. J. de Wild, G. Birant, T. Kohl, D.G. Buldu, Dr. G. Brammertz, Dr. M. Meuris, Prof. J. Poortmans, Prof. B. Vermang

C. EnergyVille 2, Thor Park 8320, 3600 Genk, Belgium

Dr. R. Thiruvallur Eachambadi, Prof. J. V. Manca

D. U Hasselt - X-LAB, Agoralaan, 3590 Diepenbeek, Belgium.

Prof. J. Poortmans

E. imec (partner in Solliance), Kapeldreef 75, 3001 Leuven, Belgium

Prof. J. Poortmans

F. Department of Electrical Engineering, KU Leuven, Kasteelpark Arenberg 10, 3001 Heverlee,
Belgium

Keywords: CIGS, alkali, elemental mapping, luminescence mapping, injection barrier

Abstract

Passivation of the Cu(In,Ga)Se₂ (CIGS) /Mo back contact using AlO_x is being investigated to reduce the recombination at this interface. In this study RbF post deposition treatment (RbF-PDT), a well-established method to improve absorber and front interface properties, is employed on these back passivated solar cells. It is found that this combination deteriorates the performance due to the formation of an injection barrier and reduced acceptor concentration. Photoluminescence yield and decay times show no indication of increased defect recombination, as both are improved. With Time of Flight - Secondary Ion Mass Spectroscopy, in-depth and lateral alkali profiles are measured. It is shown that the Na concentration is higher at the AlO_x/Mo back contact and that Rb accumulates at the CdS/CIGS interface. It is hypothesised that Na at the back is released during the RbF-PDT and inhibits the Rb diffusion into the CIGS layer. Rb remains then at the front and acceptor concentration is reduced. Modelling of dark and light current-voltage characteristics showed that the injection barrier and low doping are indeed responsible for the observed losses. It is suggested that the commonly observed fill factor losses upon heavier alkali PDT could be eliminated by adapting the initial Na amount.

1. Introduction

The Cu(In,Ga)Se₂ (CIGS) solar cell efficiency is among the highest of the thin film solar cell reaching efficiencies over 23%.^[1] As a thin film technology it has the potential to be applied in various applications requiring light weight, flexibility, semi-transparency, but also in tandem cells. The processes required to make these highly efficient solar cells can be rather complex though, making it hard to upscale. Also, the usage of the critical raw elements In and Ga raises some concern for large scale applications of CIGS technology. Both issues have encouraged research on simplified and thinner CIGS solar cell structures.^[2] An absorber layer with a

thickness of about 500 nm can theoretically achieve similar efficiency to that of a 3 μm thick absorber layer provided that the interfaces and optical path lengths are optimized.^[3]

Passivation of the Mo back contact is being investigated to reduce the recombination at the CIGS/Mo interface.^[4] This can be achieved by applying a dielectric layer between the Mo back contact and CIGS absorber layer or by implementation of a high Ga gradient at the back.^[4,5]

From upscaling perspective, applying a passivation layer is easier to achieve and is a well-known method in Si solar technology.^[2] When a dielectric is applied, the current flow may be blocked if the layer is too thick, and thus holes to connect the absorber layer with the back contact are required. These contacts have been achieved by applying nano lithography,^[6,7] nanoparticles,^[8,9] or alkali salts in the presence of Se at elevated temperatures.^[10,11]

To achieve a highly efficient absorber layer, various alkali treatments have been employed. Alkali metals are commonly added by a post deposition treatment (PDT), which involves deposition of an alkali salt (fluoride) on the grown absorber layer followed by a heat treatment. It has resulted in the most recent efficiency records and various reviews are available discussing the mechanisms behind the improvements upon (heavier) alkali treatments.^[12,13] To a lesser extent, alkali treatments have also been investigated in ultrathin CIGS solar cells.^[14–16] Though alkali treatments have led to record efficiencies, not all solar cell parameters are always improved and losses in the fill factor (FF) are often observed.^[17–23] Temperature dependent current-voltage (JV) measurements show that this may be caused by an injection barrier.^[18,24] At room temperature, an injection barrier resulting in a kink of the JV curves is generally observed upon low alkali content,^[10,25,26] or upon an unsuitable TCO.^[27,28] Few studies have shown an injection barrier at room temperature upon alkali treatments as well and this was seen when KF was used as a precursor,^[29] and upon presence of high concentration of Cs.^[23] Recently, the injection barrier upon alkali PDT has been shown by modelling to be at the CdS/ZnO interface.^[22,30] Losses in open-circuit voltage (V_{oc}) are scarcer and are attributed to

the absence of an ordered defect compound (ODC) at the CIGS surface or a too low Cu/(In+Ga) ratio.^[31,32]

In this contribution, we apply alkali treatments on AlO_x back passivated solar cells and find that this combination deteriorates the solar cell performance. An injection barrier at room temperature and losses in Voc are observed. As the passivation layer only reduces the recombination at the back contact and the alkali PDT improves the front interface and absorber layer properties, the interference of the two approaches is unexpected. Since both approaches are an obvious route towards highly efficient ultrathin CIGS solar cells, the root cause is investigated.

To understand how the RbF-PDT in combination with AlO_x passivation layer at the back deteriorates the solar cell performance, also thicker absorber layers were prepared since these suffer less from interface recombination than the thinner cells. The alkali amounts were adapted for both the thick and thin solar cells and with Time of Flight – Secondary Ion Mass Spectrometry (ToF-SIMS) lateral and in-depth elemental profiles were measured. The absorber properties were measured with hyper spectra photoluminescence (PL) imaging and time resolved PL (TR-PL). The JV characteristics were modelled using SCAPS.^[33] We will show that the performance degradation can be explained by an injection barrier at the CdS/ZnO interface and a reduction of the net acceptor concentration in the CIGS layer. Based on the lateral and in-depth elemental profiles an adapted diffusion mechanism of the alkali metals is proposed explaining the reduction of the acceptor concentration and alkali accumulation at the front.

2. Results

2.1 CIGS solar cells performance

We applied a RbF-PDT on single stage grown CIGS absorber layers. The single stage grown CIGS layers have no Ga gradient and any effects related to changes in the in-depth Ga profile

can be eliminated.^[14] However, as crystals are small ~ 100 nm,^[34] the efficiency is rather low. This also encourages an alkali PDT to improve the absorber layer quality. We prepared ultrathin CIGS layers with a thickness of 500 nm (U series) and CIGS absorber layers with a more standard thickness of 1600 nm (S series). The Na and Rb amounts were varied to have high (UH) or low (SL) amount of alkali present. The first two sets (U and S) have the same Rb/Na ratio, but differ only in CIGS layer thickness. The third set (SL) has a lower amount of Rb, but still optimized amount of Na. The fourth set had both high amount of Na and Rb for an ultrathin sample (UH). The U and SL sets had a HCl treatment before depositing the CdS layer, as this has shown to reduce the width of the injection barrier.^[18] However, the highest efficiencies were achieved without the HCl etch and since we did not observe a change in the barrier we omitted this step for the other samples. **Table 1** presents the samples that are prepared and the average solar cell parameters. The representative JV curves, doping profiles derived from capacitance-voltage (CV) measurements and TRPL data of the various samples are presented in **figure 1**.

Table 1: sample matrix and average of the solar cell parameters of the 4 different sets

Sample ^{a)}	RbF [M] ^{b)}	NaF [nm]	AlOx [nm]	V_{oc} [V]	J_{sc} [mA/cm ²]	FF [%]	η [%]
U1	-	5	-	554 ± 22	16.7 ± 0.6	65.7 ± 4.6	6.1 ± 0.7
U2	-	5	3	588 ± 8	17.7 ± 0.6	69.4 ± 2.0	7.2 ± 0.4
U3	0.2	5	-	574 ± 26	17.9 ± 0.7	65.6 ± 6.4	6.8 ± 1.1
U4	0.2	5	3	509 ± 35	20.2 ± 1.2	48.1 ± 7.7	4.9 ± 0.7
S1	-	10	-	525 ± 7	28.4 ± 2.1	57.2 ± 1.3	8.5 ± 0.7
S2	-	10	3	558 ± 8	28.8 ± 1.8	60.5 ± 0.5	9.7 ± 0.8
S3	0.4	10	-	479 ± 13	28.7 ± 2.7	51.9 ± 2.4	7.2 ± 0.9
S4	0.4	10	3	461 ± 26	27.8 ± 1.5	43.3 ± 2.8	5.6 ± 0.7
SL1	-	10	-	575 ± 23	30.9 ± 2.5	68.5 ± 2.4	12.1 ± 0.6

SL2	-	10	3	580 ± 13	29.1 ± 2.4	71.3 ± 1.8	12.0 ± 0.9
SL3	0.1	10	-	501 ± 27	32.5 ± 2.6	56.8 ± 2.5	9.3 ± 1.2
SL4	0.1	10	3	474 ± 22	29.7 ± 2.4	46.0 ± 12	6.4 ± 1.5
UH1	-	15	-	551 ± 26	21.4 ± 2.6	58.3 ± 3.3	6.9 ± 1.2
UH3	0.4	15	-	441 ± 50	18.5 ± 1.2	40.8 ± 3.3	3.4 ± 0.7

^{a)} U = ultrathin (~500 nm), S = standard thickness (1.6 μm), L = low alkali, H = high alkali; 1 = Reference, 2 = with AlO_x, 3 = with RbF, and 4 = with RbF + AlO_x; ^{b)} M is molarity spin coating solution

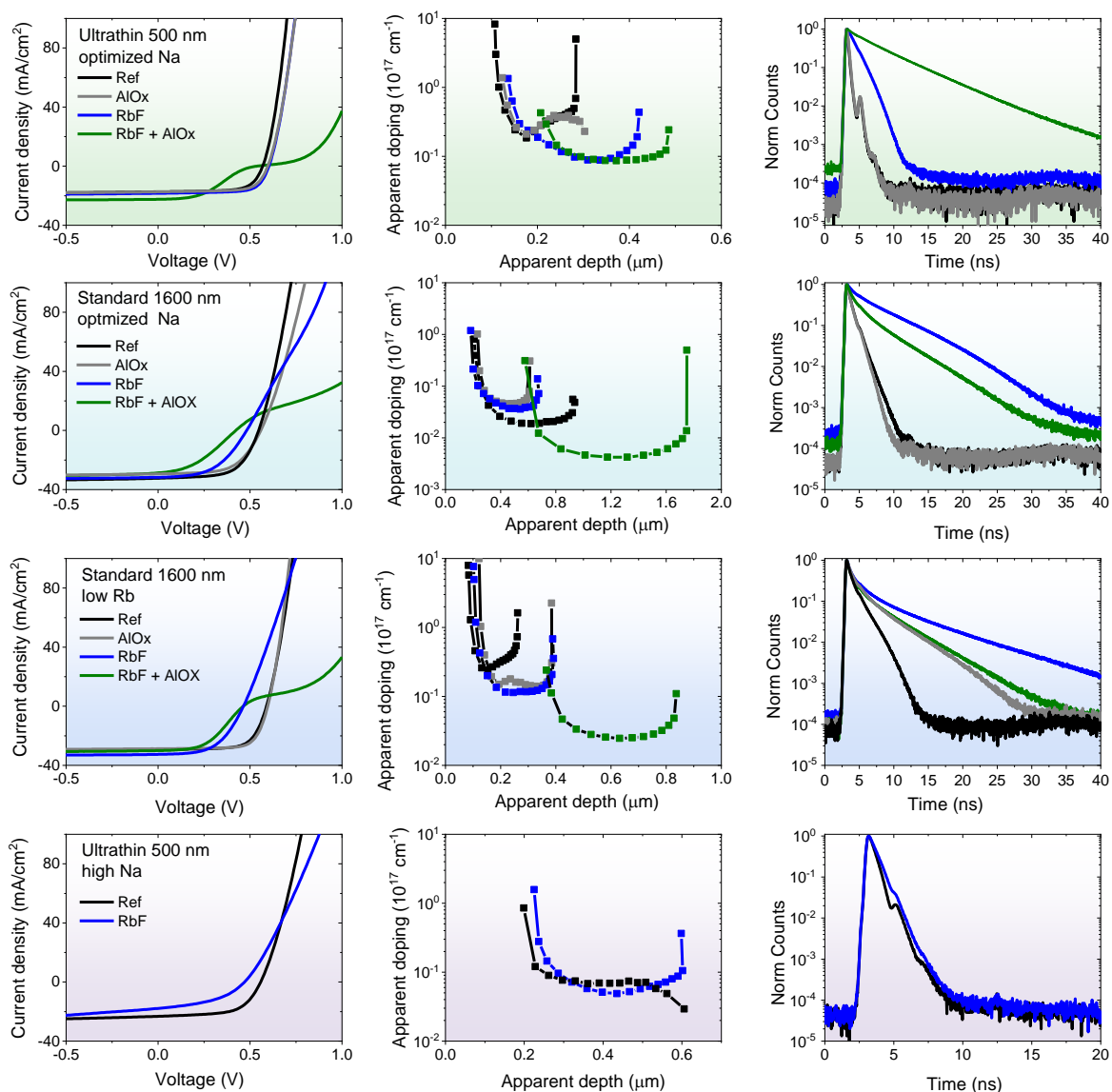


Figure 1 JV curves, doping profiles and TRPL data of the solar cells. The left column presents the JV curves, the middle column the doping profiles derived from CV measurements and the right column the TRPL data. The rows present the data in similar order as in table 1: top is the U series, below the S and SL series and bottom row presents the data of the UH series.

When looking at the results in table 1, and the JV curves presented in the left column of figure 1, we observe the following from top to bottom:

- for the U series applying RbF-PDT or AlOx layer individually improved the efficiency from about 6% to 7%. This is due to an increase in V_{oc} for RbF-PDT, and V_{oc} and FF increase for

AlOx back passivation. When both RbF-PDT and AlOx passivation layer are applied, the efficiency deteriorates to about 5%. A kink is observed and both lower Voc and FF are measured.

- for the S and SL series the AlOx layer also increases the Voc and FF. Upon RbF-PDT the solar cells degrade, which is independent on the amount of Rb. In the case of low Rb (SL) there seems to be no kink, while for standard Rb (S), there is also a small kink visible. When both RbF-PDT and AlOx passivation layer are applied a kink is clearly visible again for both S and SL series. We find that the HCl etch has no impact on the presence of this injection barrier when RbF-PDT is applied on CIGS layer with passivated AlOx back contact.

- the UH series were prepared to find how the initial amount of Na impacts the efficiency upon RbF-PDT for the ultrathin absorber layer. The reference has similar performance as that of the U series, however we find that the performance deteriorates upon RbF-PDT when high amount of Na is present. This is due to both lower Voc and FF and a significantly reduced shunt resistance. No kink is observed in this case and no HCl etch was done.

Thus, from the JV curves we find that when RbF-PDT is employed on AlOx back passivated CIGS layers an injection barrier is formed. In addition, RbF-PDT by itself may also cause degradation when a high amount of Na is initially present. We found that similar trends as described above are also observed when KF-PDT is applied to cells with AlOx at the back or high Na and when the absorber layer was grown by a 3-stage co-evaporation process on passivated back contact. These curves are presented in the supplement S1. It thus generalizes the phenomena observed above in the case of AlOx at the back or the presence of high amounts of Na.

The doping profiles are derived from the CV measurements and are presented in the second column of figure 1. We find small changes in the doping profile for all the cells upon RbF-PDT, either a decrease or increase. This is something we observed before, and it was found that it depends on the initial doping.^[16] Similar small changes are found for the AlOx solar cells compared to the reference. When RbF-PDT is applied on the AlOx passivated solar cells though,

we observe a significant decrease in the doping for all solar cells. A decrease in doping could partly explain the lower V_{oc} measured of these cells. This will be further explored in the last part upon modelling of the JV curves.

Decay curves were measured of finished solar cells to see the effect the alkali post deposition treatment has on the absorber layer properties and the CdS/CIGS interface. The decay curves are presented in the right column of figure 1. We find that all the cells that had a RbF-PDT show improved decay time, whether the back contact was passivated or not. The AlOx has only a marginal effect on the decay time. Small changes are observed between the thick and thin cells. For the thin cells the RbF-AlOx seems to have the slowest decay while for the thicker cells the RbF-PDT have the slowest decay. Despite these small differences, based on the decay curves, improvements in device performance would be expected upon RbF treatment, both for passivated and non-passivated back contact and thin and thick cells.

At last, we find that it is possible to distinguish the solar cells showing improved performance from those with deteriorated performance compared to the reference, based on optical microscopic images of the solar cells. This is presented in **figure 2**. The cells that showed improved performance with AlOx passivation layer or upon RbF-PDT look like the reference. These are shown on the left side of the red line. When the cells deteriorate, we find spots of different colours on the samples. These are shown on the right side of the red line. In the case of RbF-PDT, we see that these spots become larger when more Na was initially present. When the passivated solar cells have a RbF-PDT, spots of different colour become also visible for the U series and are larger for the S(L) series. In the next parts the effect of these inhomogeneities on the PL yield is measured by hyperspectral imaging and the origin of these spots will be explored by means of ToF-SIMS.

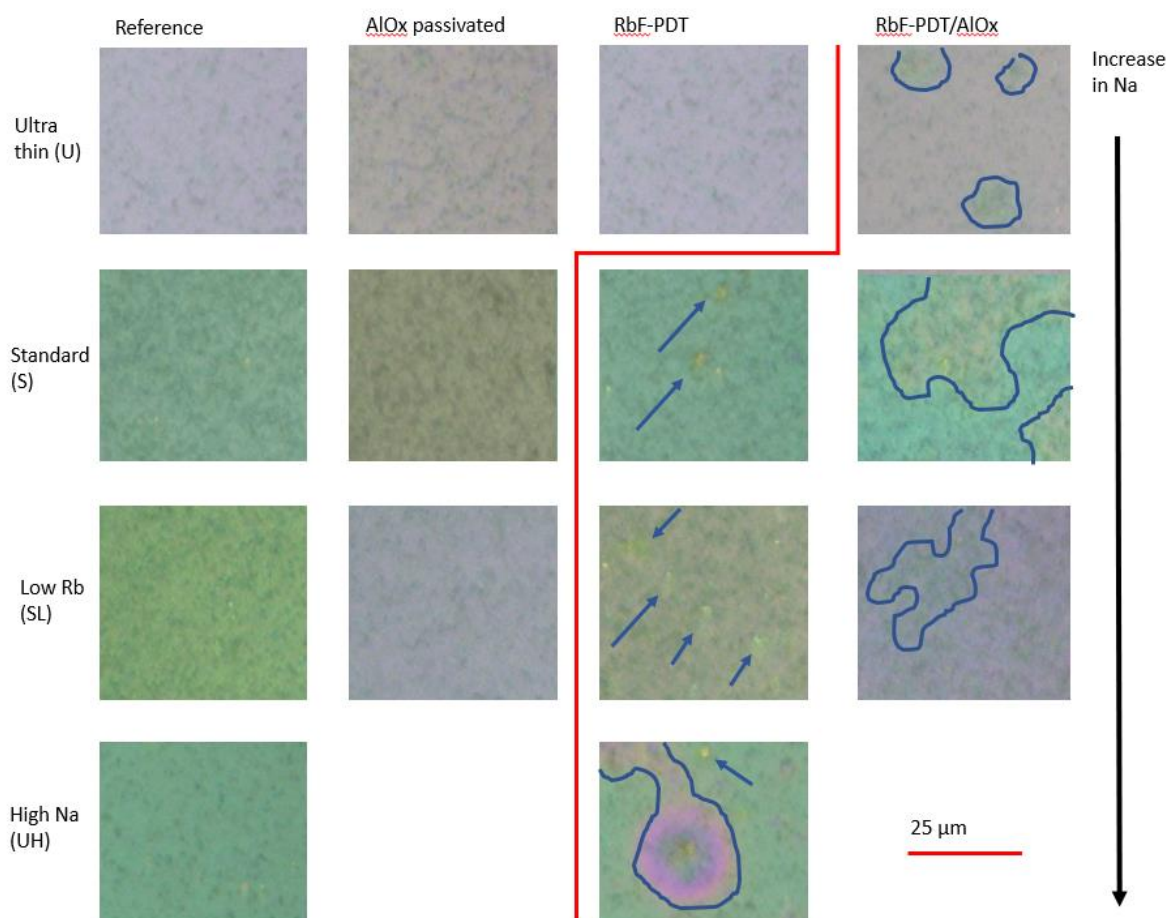


Figure 2 Microscopic images from left to right: reference, passivated, RbF-PDT and combined RbF-AlOx. From top to bottom: increase of initial NaF: 5, 10, and 15 nm NaF for U, S, SL and UH respectively. Right side of red line : devices with deteriorated performance.

2.2 Photoluminescence mapping

The samples from the S series are measured with hyperspectral imaging to see whether these spots seen in figure 2 impact the PL yield. With hyperspectral imaging, a large area is illuminated, and the PL and reflection spectra are collected in grids of $1 \times 1 \mu\text{m}^2$ and presented as a pixel in a colour coded map. Each pixel in the map presents the counts at a specified wavelength. **Figure 3** presents the maps and PL and reflection spectra of the reference, RbF-PDT and RbF-AlOx of the S series. In general, the single stage PL spectra are heavily

influenced by interference which we have shown before for the ultrathin samples.^[35] As these layers are 1600 nm thick, even more fringes are present. The peak at 1050 nm is due to neodymium in the microscope objective being excited by the laser. The maps show therefore the intensity measured at 1101 nm eliminating this optics-related peak at 1050 nm. The blue areas are the grids.

When looking at the reference sample, we find that the PL intensity is rather homogeneous. No distinguishable features or structures are seen, except higher intensity closer to the grids. When looking at the individual PL spectra of a high and low intensity area, presented below the map, this homogeneity is confirmed. Similar conclusion was drawn for ultrathin single stage samples.^[35] Also presented is the peak at 1050 nm, measured at the grid (blue area). When looking at the maps of the RbF-PDT solar cell, we see some small red spots of the size of a few microns. These could indeed be the spots seen in the optical microscopic images. From the individual spectra, plotted in the graph below, we find that the difference in intensity varies up to a factor 2 at 1101 nm. The intensity is in general higher than that of the cell without RbF. Higher intensity means less non-radiative recombination in the cell and is consistent with the higher decay times measured before (figure 1). When measuring the RbF/AlO_x cell, presented rightmost in figure 3, we find large ring-shaped spots and even larger differences in intensity. We believe these are again related to the spots seen in the micrographs, figure 2. The ring has the highest intensity, and the inner area has a slightly lower intensity. Between the rings, the intensity is the lowest. The intensity is in general higher than the reference and the RbF-PDT solar cell. An increase up to a factor of four was measured for the ring-shaped areas when compared to the reference. This again implies that the recombination in the CIGS layer and/or at the CdS/CIGS interface is reduced.

Based on the TRPL and PL data presented above, an increase in V_{oc} would thus be expected upon RbF-PDT with and without AlO_x at the back. However, it is also known that lateral

inhomogeneities are a source for Voc losses as well.^[36] To understand where the inhomogeneities come from, the chemical composition of various solar cells is measured.

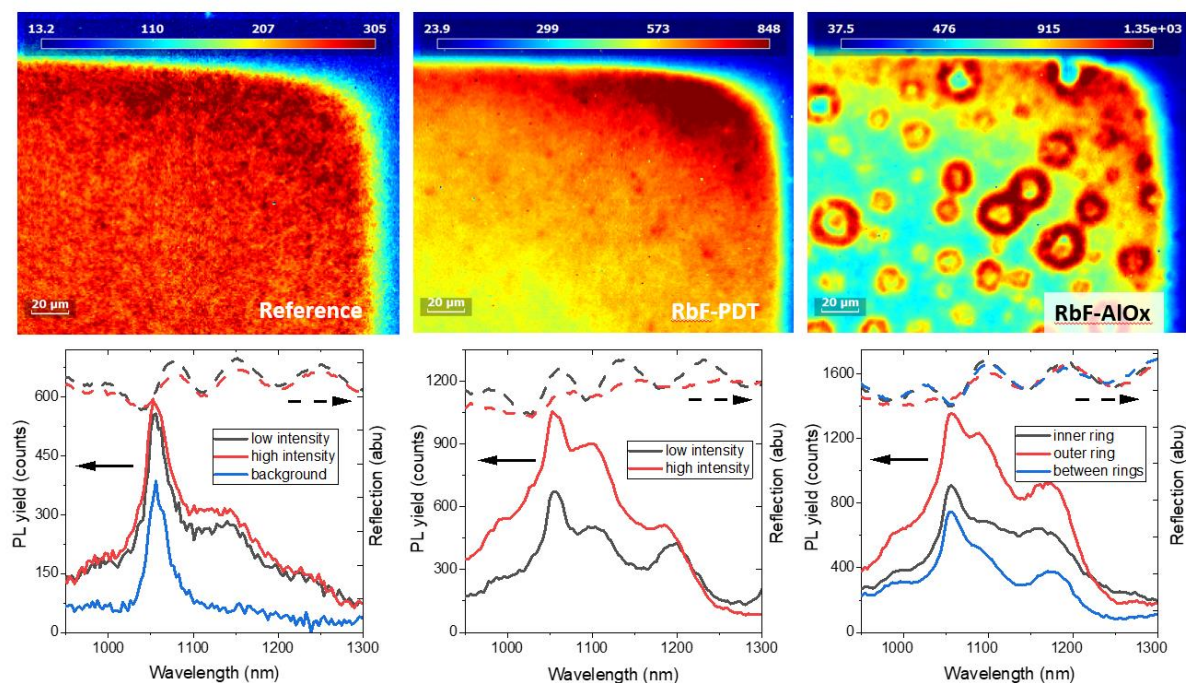


Figure 3 Top: the intensity maps of the PL at 1101 nm, from left to right: reference, RbF-PDT and RbF-AlOx of the S series. Bottom: spectra of high intensity and low intensity area from the maps presented above. The peak observed at ~1050 nm is due to neodymium in the microscope objective being excited by the 532 nm laser. The reflection spectra is normalized with the lamp spectrum and shifted in height to accommodate both the PL and reflection spectra.

2.3 Compositional analysis and elemental mapping

In-depth elemental profiles of selected samples (S and UH samples) were measured with ToF-SIMS. **Figure 4** presents the profiles of the various alkali metals. The Cu, In and Ga profiles are flat and examples of those graphs can be found in the supplement S2. The sputter times are adapted in such a way that the Cd peaks at the front and Mo/(Al) at the back of the difference samples are overlapping. At first sight, the alkali profiles and the changes observed upon RbF-PDT are consistent with literature: the alkali metals accumulate at the CdS and Mo(Al) interfaces and after PDT with heavier alkali, the lighter alkali is reduced.^[18,24,37–39]

When comparing the alkali between cells with and without AlOx at the back, shown in figure 4a and b as solid lines, we find that the Na counts are about 1 order higher when AlOx is present at the back. This is unexpected, since in both cases 10 nm NaF was evaporated at room temperature before CIGS growth. It could be that less Na is present on Mo compared to AlOx when the substrate temperature is increased to 550 °C. This implies that some of the Na evaporates when the substrate temperature is increased, and this amount is different when AlOx is present. We hypothesize that this has to do with the AlOx layer which is grown by ALD, which has not been annealed when the NaF is evaporated and is thus amorphous.^[40,41] The NaF may have better adhesion on this amorphous AlOx layer compared Mo. Upon heating the substrate a bit of NaF may evaporate, but less when NaF is deposited on the AlOx layer. When the CIGS is grown, more Na is then present to diffuse into the CIGS layer compared to Mo.

When RbF-PDT is applied, we see differences in both the Rb and Na counts and profiles, see figure 4a and b dashed lines. When there is no AlOx at the back, the Na is almost depleted at the back, and at least 1 order lower than at the front. The Na profile of the back passivated cell looks rather flat through the layer and even increases a bit towards the front. It seems that the Na present at the AlOx/Mo back contact is also diffusing into the absorber layer during the PDT and thus the back is not depleted of Na. At the CdS layer there is a steep increase in Na. This absolute increase is likely due to matrix effect as the environment changes from CIGS to CdS.^[42] However, it probably means that there is Na in the CdS layer. This is in contrast to the profiles that directly go down at the CdS/CIGS interface.

The Rb profiles look initially rather similar for both cells. Closer look reveals that the counts are higher for the reference, while the passivated cell has a steeper increase of Rb at CdS/CIGS interface. It seems that the Na coming from the AlOx/Mo back contact inhibits the diffusion of Rb from the front into the absorber layer. Rb then accumulates at the front.

The profiles described above are based on at least 2 spots of 100x100 μm^2 and no significant differences were found. This is different for the high alkali series (UH), where we see that Na

profiles change from spot to spot. This is presented in figure 4c and d. One spot follows the typical Na profile: slow increase towards the back. The other spot shows a small Na accumulation in the CdS layer. After RbF-PDT, we find that the Rb profiles overlap, but also that the counts saturate halfway the absorber layer. The amount of Rb diffusing into the absorber layer is thus significantly larger than that of the thick samples, which we believe is due to the initial higher amount of Na in the absorber layer. It is known that if Na is already present in the absorber layer, the Rb diffusion coefficient is increased along the grain boundaries, while inhibiting the diffusion of Rb into the grains.^[43] This is not the same as the case that Na comes from the AlOx/Mo back contact. These atoms were not present in the absorber layer prior to the PDT. Looking at the Na profiles after RbF-PDT, we find again that the profiles differ per spot. Thus, the high amount of Na leads to large lateral differences in Na concentration both before and after RbF-PDT.

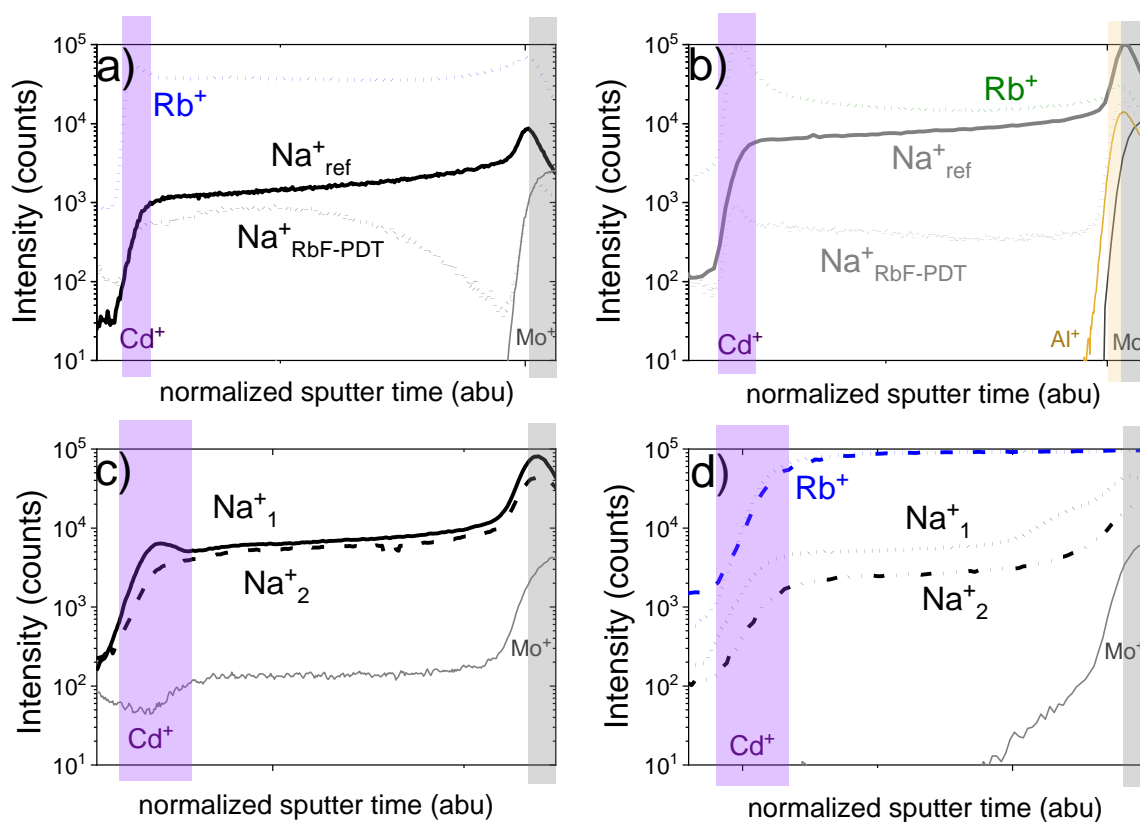


Figure 4 ToF-SIMS depth profiles of the alkali elements. From the S series: a) reference solar cells with and without RbF-PDT; b) Back passivated solar cells with and without RbF-PDT.

From the UH series: c) ultrathin solar cell with high amount of Na and d) ultrathin solar cells with high amount of Na and RbF-PD. The profiles are aligned to the Cd peak at the front and Mo (Al) at the back.

When AlOx is deposited at the back, holes are formed in the layer during CIGS growth in the presence of NaF.^[11] To see how this impacts the alkali profiles laterally, the samples from the S series with AlOx at the back were also measured with high lateral resolution ToF-SIMS. For this the counts of selected elements are added in a region close to the CdS and AlOx layer (supplement S3). **Figure 5** presents the maps of representative elements at the back contact (CIGS/AlOx/Mo) and front interface (CIGS/CdS).

We find that the holes in the AlOx layer are clearly identifiable in the Al map, even though the layer is only 3 nm thin. It is also shown that Na content is higher when the AlOx layer is present, and the Na and Al maps show similar pattern. Thus, as hypothesised earlier, Na accumulates at the AlOx/Mo interface. A similar finding was observed in the presence of AlOx nanostructures, in which an accumulation of Na at the CIGS/Mo interface was found.^[44] At the front (CdS/CIGS interface) we find that the Na is rather homogenous again. Also, Ga variations are observed, both at the front and the back. This could be due to the interaction between Na and Ga.^[45-47] Maps of Cu, In, (front/back) Cd and Zn are shown in the supplement S4.

The maps of the RbF/AlOx solar cell of the S series are presented in **figure 6**. Here we also see that at the back the Na and Al maps overlap. Rb seems to follow a similar profile as that of Na/Al but to a lesser extent. At the CdS/CIGS interface large variations in Rb counts are visible though. These variations seem to be weakly correlated with the Na profile at the back. At the bottom right of the Na map of the back contact, we see that there is a slightly lower amount of Na, while at the front the Rb counts are significantly higher in this area. This indeed corresponds with the finding earlier, that less Na causes less Rb diffusion into the absorber layer. When the

Rb is not diffusing into the absorber layer, it accumulates at the front and we thus see an anti-correlation between Na at the back and Rb at the front.

When the Rb accumulates at the front, a significant depletion of Ga is seen. This depletion is on top of the smaller variations already seen for the AlO_x solar cell. The finding that Rb causes Ga depletion at the front has been observed before.^[22,38,48] However, from these maps it seems that this is induced by lateral Na inhomogeneities at the back. These areas with higher counts of Rb are likely related to the areas in which the PL yield was higher. The rings are about 10 to 20 μm in diameter, so is the area where we see Rb accumulation and Ga depletion. The higher PL yield at this position, fits the consensus that lower Ga and the presence of Rb phases reduces recombination at the CdS/CIGS interface.

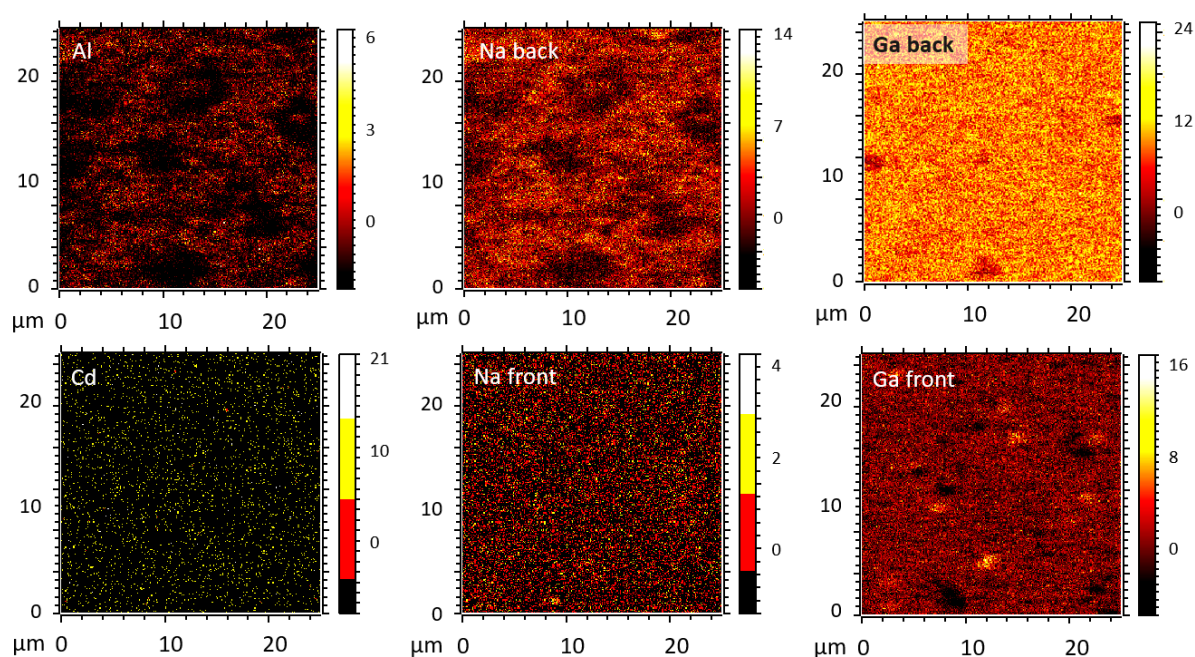


Figure 5 ToF-SIMS maps of 25x25 μm² area with high lateral resolution of the AlO_x passivated solar cell from the S series. Figures with very low counts have increased contrast. Top: elemental maps of Al, Na and Ga at the back contact. Bottom: elemental maps of Cd, Na and Ga at the front.

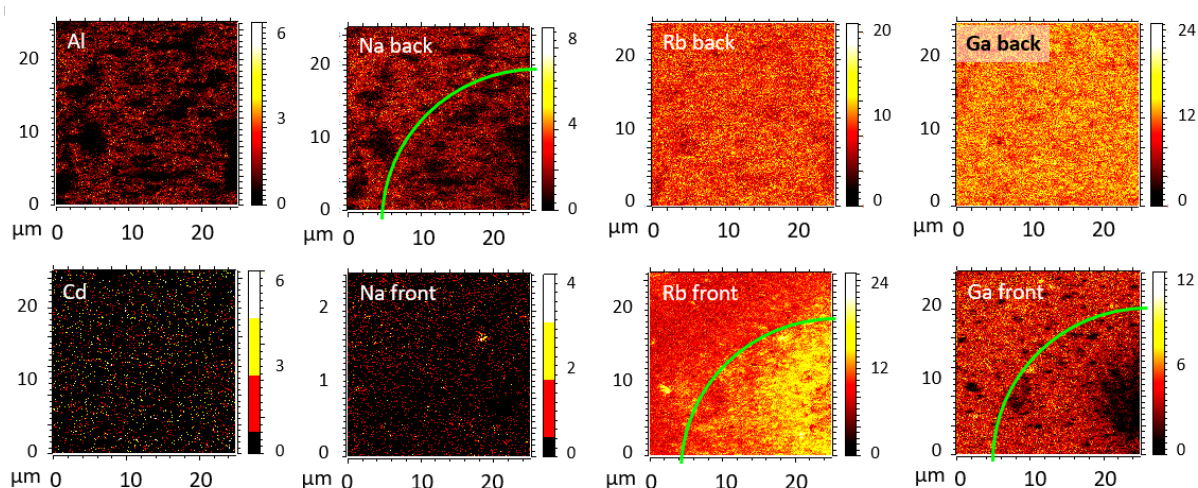


Figure 6 ToF-SIMS maps with high lateral resolution of the RbF-AlO_x solar cell from the S series. Figures with very low counts have increased contrast. Top: elemental maps of Al, Na, Rb and Ga at the back contact. Bottom: elemental maps of Cd, Na, Rb and Ga at the front. The green curved line encloses the bottom right region in the maps showing a slightly lower amount of Na at the back, a Rb accumulation at the front and a significant depletion of Ga at the front.

3. Discussion

The first part of the discussion will provide a model about the diffusion of the alkali, based on existing literature and the new findings related to the Na accumulation at the AlO_x/Mo back contact. A reason for the low doping and formation of the barrier will be proposed. In the second part, we will model the measured JV curves taking the presence of a barrier at the CdS/ZnO interface into account.

3.1 Interaction between Na and Rb

The schematic presentation of the proposed diffusion mechanism can be found in **figure 7**. At the top, the diffusion is presented as generally accepted, based on literature. At the bottom a new model is proposed, based on the hypothesis that the AlO_x/Mo back contact suffices as Na source. We will take 3 kinds of elements into account, that is Rb, Na and the copper vacancy (V_{Cu}). The copper vacancies are the main source of the p-type doping in CIGS which is known

to be influenced by Na. In the case of RbF-PDT without AlOx at the back the steps of Rb diffusion into the CIGS layer are:

1a → 2a) Rb is applied on top of the CIGS layer. Upon heating it diffuses into the absorber layer via the grain boundaries^[43]. Na diffuses out of the absorber layer via the grain interior and grain boundaries, reducing the amount of Na in the absorber layer^[43,49]

2a → 3a) During cooling down the lower amount of Na that is left in the absorber layer is pushed out of the grain interior to the grain boundaries if possible or remains in the grain changing the concentration of the copper vacancies.^[50] As it is known that the net acceptor concentration in the CIGS layer is highly dependent on the copper vacancies, changes in doping can be expected on small variations in the concentration of the copper vacancies.

When AlOx is applied at the back we also have a source of Na at the back. Thus when Rb diffuses according to the process described above into the absorber layer, Na will also diffuse into the absorber layer from the back. The following added mechanisms are proposed:

1b → 2b) Rb/Na exchange at the front is similar as in 2. Additionally, a high concentration of Na is present at the back of the CIGS absorber layer. Na diffuses from the back into the absorber layer during the PDT. The reduction of Na will be less and the concentration of copper vacancies will change.

2b → 3b) The ratio between Na and the copper vacancies has changed. In addition, Rb is diffused into the absorber layer as well. The concentration of Na is significantly higher than in situation 2/3 and cannot all be expelled from the grain interior to the grain boundaries as there will be the Rb. As it is proposed that expelling Na from the grain interior leaves copper vacancies behind, we propose that leaving the Na in the grain, the concentration of copper vacancies reduces. As the copper vacancy is considered to be the main acceptor in CIGS, reducing the copper vacancies will drastically decrease the doping.

To explain the formation of the barrier, we will look again at figure 4b. We find that the barrier/kink in the JV curve coincides with an increase of Rb at the CdS/CIGS interface. It is

likely that the CdS layer contains Rb in these cases. The origin of the high amount of Rb at the top surface, can be explained by the interaction of Rb diffusion into the absorber layer in the presence of Na diffusion from the back. When there is diffusion of new Na from the back into the absorber layer, the diffusion of Rb into the absorber layer is inhibited. This indeed leads to a slightly lower amount of Rb in the absorber as observed in figure 4b, but also higher amount of Rb at the front. During the chemical bath deposition of the CdS layer, only a part is removed and a part of the alkali remains and goes into the CdS layer. It is known that alkali in CdS and ZnO layers can form acceptor states, which cause the observed barrier at the CdS/ZnO interface.^[22]

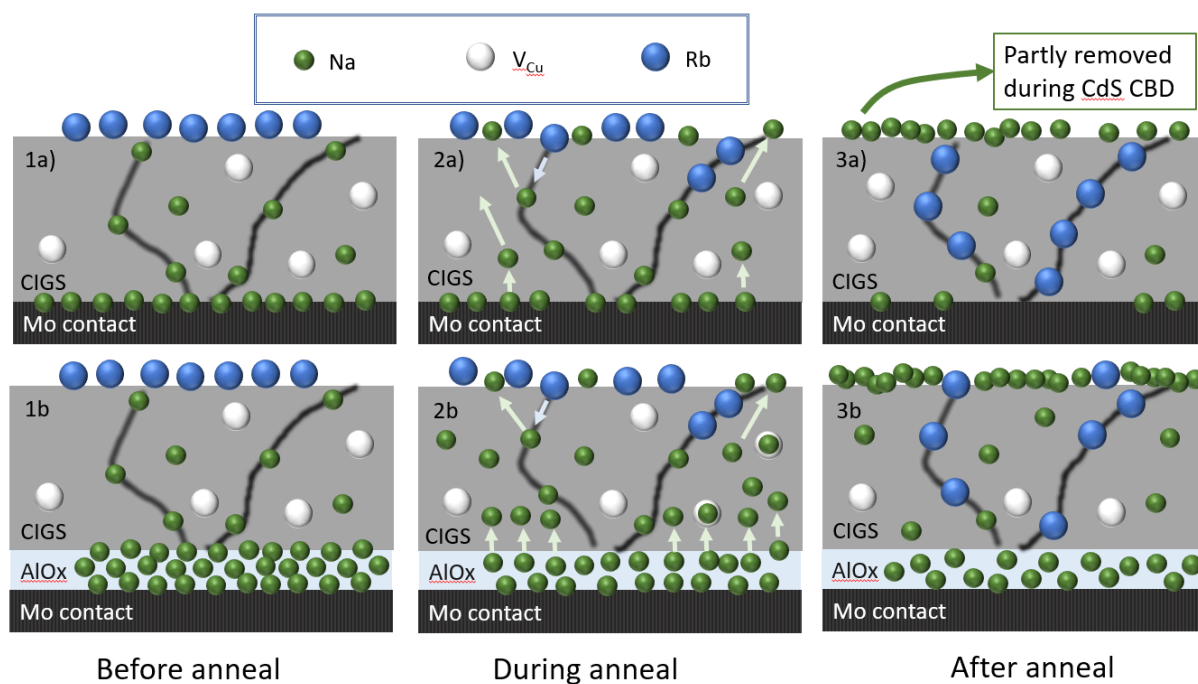


Figure 7 Proposed mechanism of the effect of RbF-PDT in the presence of an AlO_x passivation layer at the back. Top: the mechanism as proposed in literature, bottom: the adapted mechanism in the presence of AlO_x at the back. 1a) and b) alkali distribution before anneal, 2a) and b) alkali exchange during anneal, 3a) and b) alkali distribution after cooling down.

3.2 JV curves modelling

In the previous sections we found that combining RbF-PDT on AlO_x back passivated solar cells cause an injection barrier, large-scale variations in composition at the CIGS interfaces and low doping. This barrier is not removed by an HCl etching step. Instead, the origin seems to lie in the presence of Na at AlO_x/Mo back contact which causes competing diffusion mechanisms during the PDT and alkali accumulations at the CdS/CIGS interface. In this part we will model the measured JV curve taking into account the anticipated changes at the CdS/ZnO interface to gain more insight in the origin of the Voc and FF losses. We used the 1D program SCAPS.^[33] It does not allow modelling of 2D structures, thus we cannot model the lateral inhomogeneities found at the CdS/CIGS and back interface.

The JV curve of the ultrathin sample (U series) with AlO_x and RbF-PDT will be simulated, since this sample shows the sharpest kink. **Figure 8** top presents the simulated and measured light and dark curves. The modelling parameters can be found in supplement S5. We find that a kink can be simulated by applying acceptor defects, but also a thin (2 nm) barrier with lower electron affinity.^[22,30] The shape of the kink can easily be adapted by changing the doping of the CdS layer in general and the concentration and energy position of the acceptor defects, or the electron affinity and the band gap of the barrier.^[30]

It is clear from figure 8a that both defects and a barrier can model the light JV curves very well. However, there is a mismatch with the dark curve for both models, see figure 8b. This mismatch seems to be reduced when modelling the dark curve using both the defects and a barrier. However, now the light curve shows a mismatch. This mismatch between dark and light curves is commonly observed in thin film solar cells though. In the case of CIGS it is caused by light induced defects, most likely at the CdS/CIGS interface.^[51–53]

To have a closer look into this change from dark to light, also the intensity dependence of the barrier, the defects, and the combination on the Voc and Jsc is simulated. The results are presented in figure 8c, the star presents the 1 sun intensity. We find that the Voc in presence of

defects suffers most from the change in intensity, while the barrier itself does not seem to be affected by the light intensity. The combined approach on the other hand, is the most affected by changing the light intensity. This is also what we observe in our solar cells. Figure 8d shows the J_{sc}/V_{oc} data of an AlOx/RbF cell and its AlOx reference from the SL series. The stars are again the measurements under 1 sun. The straight line is a simple 1 diode fit for the linear part: $V_{oc} = \frac{k_B T n}{q} \ln \left(\frac{I_{sc}}{I_0} - 1 \right)$. We find a diode factor of 1.6 and 1.8 and a I_0 of $1.8 \cdot 10^{-8}$ and $2.3 \cdot 10^{-7}$ A for the AlOx and RbF-AlOx solar cell respectively. Comparing these linear fits, we observe at 1 sun a shift of about 50 mV towards lower V_{oc} due to the higher I_0 and a reduction of about 40 mV due to the barrier/defects at the CdS/ZnO interface.

Since the I_0 is dependent on many variables, among which the doping, we will determine the V_{oc} losses expected based on the measured reduction in the acceptor concentration.^[54] The doping profiles are presented in figure 1 and taking the lowest values we find $N_{A_AlOx} = 1.4 \cdot 10^{16} \text{ cm}^{-3}$ and $N_{A_RbF-PDT} = 2.4 \cdot 10^{15} \text{ cm}^{-3}$. The change in V_{oc} due to the changes in the doping can then be calculated with $\Delta V_{oc} = \frac{k_B T}{q} \ln \left(\frac{N_{A_Ref}}{N_{A_RbF-AlOx}} \right)$ and gives 45 mV. The shift of about 50 mV can thus largely be attributed to the change in doping.

From this modelling, almost all the V_{oc} losses can be attributed to the barrier and lower doping. It therefore seems that the lateral inhomogeneities observed in the ToF-SIMS and hyperspectral imaging are only marginally responsible for the V_{oc} losses. However, considering the increase in lifetime and PL yield, an increase in V_{oc} should have been observed. A PL yield increase of about 4 times, as seen in the hyperspectral imaging, should increase the V_{oc} about 30 to 40 mV. On the other hand, band gap and electrostatic fluctuation decrease the band gap again.^[36] Thus, any improvement in the CIGS layer and/or at the CIGS/CdS interface might have been nullified by the observed inhomogeneities. This could explain why there are still large V_{oc} losses upon RbF-PDT in the presence of high amounts of Na even though the changes in doping are

relatively small. At this stage it is hard to exactly anticipate the effect of the inhomogeneities observed in composition and PL yield on the V_{oc} though.

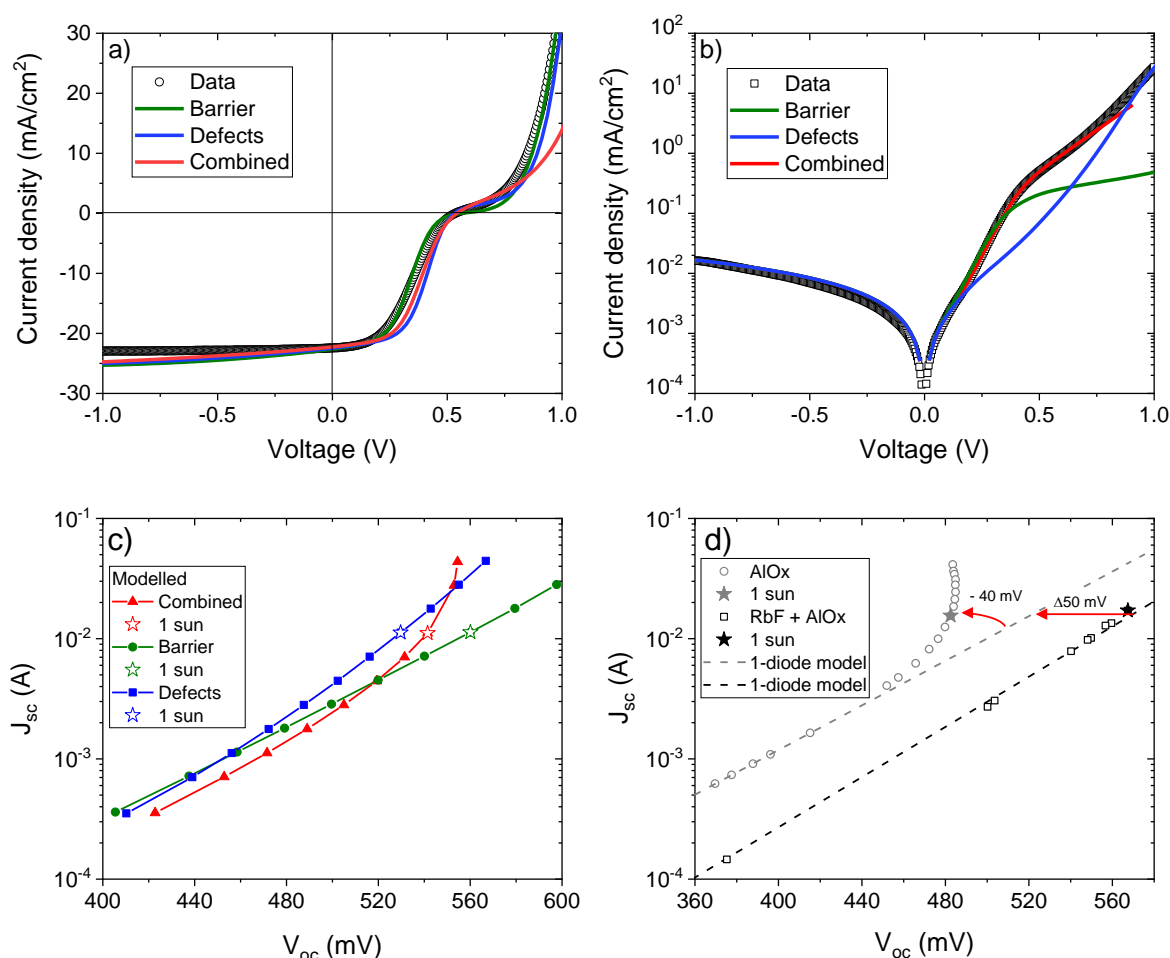


Figure 8 Simulated and measured JV curves and J_{sc} - V_{oc} curves. a) light curves with barrier, defects or combined, b) similar as a but for the dark curves of the S series c) simulated intensity dependence of the J_{sc} and V_{oc} and d) intensity dependence of V_{oc} and J_{sc} of RbF-AlOx and AlOx solar cell from the SL series

4. Conclusion

We have shown that applying RbF-PDT on AlOx back passivated solar cells results in decreased solar cell performance. There seem to be several causes at play here. The first is the formation of a barrier at the CdS/ZnO interface reducing the FF. This has been observed before,

except that the barrier usually only appears at lower temperatures. It does explain the commonly observed FF losses at room temperature though. Secondly, we found a large reduction of doping. The effect of the lower doping and barrier on the Voc could be disentangled by means of modelling the JV curves and light intensity dependent measurements. At last, using in-depth and lateral elemental mapping we found that inhomogeneities occur at the back due to the presence of AlOx and at the front due to Rb accumulation and Ga depletion induced by the AlOx layer. These inhomogeneity do not seem to affect the TRPL and PL negatively as those are improved for all RbF treated solar cells. How much these inhomogeneities contributed to the measured losses in the device remains unknown. That this also causes losses is inferred from the fact that there was a direct correlation between solar cells suffering from Voc losses and visible inhomogeneities.

Based on the elemental depth profiles and mapping we provided an explanation on why the doping is reduced upon RbF-PDT when AlOx is deposited at the back. The main source seems to be the release of Na from the AlOx/Mo back contact during the PDT. Based on the findings in this study, we encourage to also optimize the initial Na amount when heavier alkali PDTs are applied. It might resolve the FF losses commonly observed upon the heavier alkali PDT and thus increase the efficiency even further.

5. Experimental Section/Methods

The CIGS layers are grown on a soda lime glass/Mo substrate with ~ 100 nm Si(O,N) alkali barrier between the Mo and glass. The amount of alkali metals is thus externally controlled. Na is added before CIGS growth by evaporating NaF on the Mo(/AlOx) substrate. The thickness was measured by a quartz crystal sensor. A CIGS layer of 500 or 1600 nm is grown by single stage co-evaporation with a $[Cu]/([Ga]+[In])$ of ~ 0.8 and $[Ga]/([Ga]+[In])$ of 0.3, measured with XRF. The alkali-PDT is done by spin-coating RbF (KF) solution and anneal at 350 (400) °C for 20 minutes under a cover in N₂ atmosphere. The details are described elsewhere.^[14] HCl

dip was done at room temperature in 10% HCl for 1 minute for the SL and U series. As this did not change the barrier, it was omitted for the other samples (incl. those in supplement). Solar cells were prepared by chemical bath deposition of CdS buffer layer, followed by sputtering of 50 nm ZnO. As TCO layer either sputtered AZO (300 nm) for the U and SL series or sputtered ITO (150 nm) for the S and UH series was used. The metal contacts were made by evaporation of Ni/Ag/Ni. The AlO_x passivation layer of 3 nm was deposited through atomic layer deposition (ALD) at 300°C. During the deposition, trimethylaluminum (TMA) was used as the precursor and H₂O used as reactant. The holes in the AlO_x layer to make electrical contact with Mo are formed during CIGS growth in combination with the NaF and Se. Details on the formation of the contacts and ALD deposition can be found elsewhere.^[11]

The solar cells were measured with a Keithley 2400 source meter using four-point probe under A.M. 1.5 spectra. The intensity was calibrated with a Si reference cell. Light intensity was further varied using neutral density filters for lower than 1 sun and by increasing the intensity of the xenon lamp up to 3 suns. The JV curves were modelled using 1D SCAPS program. The input parameters can be found in the supplement. The doping in the CdS layer, defect concentration, and barrier height at CdS/ZnO were varied to model the measured JV curves. The capacitance-voltage data was acquired with an Agilent E4980A Precision LCR Meter. The tool is equipped with a built-in 40Vdc bias option, allowing for the measurement under different bias conditions. We have varied the bias voltage from -1 V to +1 V in 21 steps. Doping profiles are presented at a frequency of 100 kHz.

The TRPL of the finished solar cells was acquired with a Picoquant FluoTime 300 system, the excitation wavelength was 532 nm, time resolution 25ps and repetition rate 3MHz. Microscopic images were taken with Keyence confocal microscope under 50x magnification. Hyperspectral imaging was done by a global hyperspectral imager (IMA; Photon etc., Canada). The samples were homogeneously excited with a 532 nm laser, and the optical and PL images were acquired with an InGaAs camera. The intensity was 800 mW, spectral resolution 3 nm, field of view

384x480 μm^2 and lateral resolution 2.2 μm . The reflectance data was normalized to the lamp spectrum. ToF-SIMS measurements were performed using ION.TOF NCS instrument (IONTOF GmbH, Muenster, Germany). Sputtering was carried out with a 2 keV O_2 ion beam. The sputter area of 350x350 μm^2 , and an analysis area of 100x100 μm^2 was used for the depth profiles, with a raster of 128x128 pixels. 15 keV Bi^+ was used as analysis beam. For high lateral-resolution measurements, sputter area was 100x100 μm^2 and analysis area was 25x25 μm^2 . The analysis source was Bi^+ 30 keV with a raster size of 256 x 256 pixels, and a delayed extraction time of 85 ns was used.

Supporting Information

Supporting Information is available from the Wiley Online Library or from the author.

Acknowledgements

The work published in this paper was supported by the European Research Council (ERC) under the Union's Horizon 2020 research and innovation program (grant agreement No 715027).

We thank Photon etc. for the hyperspectral measurements.

RTE and JM were supported by the Research Foundation – Flanders (FWO) (grant number: G031416N). ToF-SIMS was rendered possible thanks to a grant awarded to UHasselt and imec by Hercules Foundation (now FWO, grant number: ZW/13/07, awarded to JM, among others).

Received: ((will be filled in by the editorial staff))

Revised: ((will be filled in by the editorial staff))

Published online: ((will be filled in by the editorial staff))

References

- [1] M. Green, E. Dunlop, J. Hohl-Ebinger, M. Yoshita, N. Kopidakis, X. Hao, *Progress in Photovoltaics: Research and Applications* **2021**, *29*, 3.
- [2] B. Vermang, J. T. Wätjen, V. Fjällström, F. Rostvall, M. Edoff, R. Kotipalli, F. Henry, D. Flandre, *Progress in Photovoltaics: Research and Applications* **2014**, *22*, 1023.
- [3] M. Gloeckler, J. R. Sites, *Journal of Applied Physics* **2005**, *98*, 103703.
- [4] G. Birant, J. de Wild, M. Meuris, J. Poortmans, B. Vermang, *Applied Sciences (Switzerland)* **2019**, *9*.
- [5] L. M. Mansfield, A. Kanevce, S. P. Harvey, K. Bowers, C. Beall, S. Glynn, I. L. Repins, *Progress in Photovoltaics: Research and Applications* **2018**, *26*, 949.
- [6] S. Bose, J. M. V. Cunha, S. Suresh, J. De Wild, T. S. Lopes, J. R. S. Barbosa, R. Silva, J. Borme, P. A. Fernandes, B. Vermang, P. M. P. Salomé, *Solar RRL* **2018**, *2*.
- [7] P. M. P. Salomé, B. Vermang, R. Ribeiro-Andrade, J. P. Teixeira, J. M. V. Cunha, M. J. Mendes, S. Haque, J. Borme, H. Águas, E. Fortunato, R. Martins, J. C. González, J. P. Leitão, P. A. Fernandes, M. Edoff, S. Sadewasser, *Advanced Materials Interfaces* **2018**, *5*, 1701101.
- [8] B. Vermang, V. Fjällström, X. Gao, M. Edoff, *IEEE Journal of Photovoltaics* **2014**, *4*, 486.
- [9] B. Vermang, J. T. Wätjen, V. Fjällström, F. Rostvall, M. Edoff, R. Gunnarsson, I. Pilch, U. Helmersson, R. Kotipalli, F. Henry, D. Flandre, *Thin Solid Films* **2015**, *582*, 300.
- [10] D. Ledinek, O. Donzel-Gargand, M. Sköld, J. Keller, M. Edoff, *Solar Energy Materials and Solar Cells* **2018**, *187*, 160.
- [11] G. Birant, J. de Wild, T. Kohl, D. G. Buldu, G. Brammertz, M. Meuris, J. Poortmans, B. Vermang, *Solar Energy* **2020**, *207*, 1002.
- [12] S. Siebentritt, E. Avancini, M. Bär, J. Bombsch, E. Bourgeois, S. Buecheler, R. Carron, C. Castro, S. Duguay, R. Félix, E. Handick, D. Hariskos, V. Havu, P. Jackson, H.-P. Komsa, T. Kunze, M. Malitckaya, R. Menozzi, M. Nesladek, N. Nicoara, M. Puska, M. Raghuvanshi, P. Pareige, S. Sadewasser, G. Sozzi, A. N. Tiwari, S. Ueda, A. Vilalta-Clemente, T. P. Weiss, F. Werner, R. G. Wilks, W. Witte, M. H. Wolter, *Advanced Energy Materials* **2020**, *10*, 1903752.
- [13] R. Carron, S. Nishiwaki, T. Feurer, R. Hertwig, E. Avancini, J. Löckinger, S.-C. Yang, S. Buecheler, A. N. Tiwari, *Advanced Energy Materials* **2019**, *9*, 1900408.
- [14] J. de Wild, D. G. Buldu, T. Schnabel, M. Simor, T. Kohl, G. Birant, G. Brammertz, M. Meuris, J. Poortmans, B. Vermang, *ACS Appl. Energy Mater.* **2019**, *2*, 6102.
- [15] J. de Wild, M. Simor, D. G. Buldu, T. Kohl, G. Brammertz, M. Meuris, J. Poortmans, B. Vermang, *Thin Solid Films* **2019**, *671*, 44.
- [16] J. De Wild, T. Kohl, D. G. Buldu, G. Birant, D. M. Parragh, G. Brammertz, M. Meuris, J. Poortmans, B. Vermang, *IEEE Journal of Photovoltaics* **2020**, *10*, 255.
- [17] S. Karki, P. Paul, G. Rajan, B. Belfore, D. Poudel, A. Rockett, E. Danilov, F. Castellano, A. Arehart, S. Marsillac, *IEEE Journal of Photovoltaics* **2019**, *9*, 313.
- [18] T. P. Weiss, S. Nishiwaki, B. Bissig, R. Carron, E. Avancini, J. Löckinger, S. Buecheler, A. N. Tiwari, *Advanced Materials Interfaces* **2018**, *5*, 1701007.
- [19] M. Balestrieri, V. Achard, T. Hildebrandt, L. Lombez, M. Jubault, S. Béchu, M. Bouttemy, A. Etcheberry, D. Lincot, F. Donsanti, *IEEE Journal of Photovoltaics* **2018**, *8*, 1343.
- [20] N. Nicoara, T. Lepetit, L. Arzel, S. Harel, N. Barreau, S. Sadewasser, *Scientific Reports* **2017**, *7*, 41361.
- [21] P. Pistor, D. Greiner, C. A. Kaufmann, S. Brunken, M. Gorgoi, A. Steigert, W. Calvet, I. Laueremann, R. Klenk, T. Unold, M.-C. Lux-Steiner, *Appl. Phys. Lett.* **2014**, *105*, 063901.
- [22] T. Kodalle, M. D. Heinemann, D. Greiner, H. A. Yetkin, M. Klupsch, C. Li, P. A. van Aken, I. Laueremann, R. Schlatmann, C. A. Kaufmann, *Solar RRL* **2018**, *2*, 1800156.
- [23] T.-Y. Lin, I. Khatri, J. Matsuura, K. Shudo, W.-C. Huang, M. Sugiyama, C.-H. Lai, T. Nakada, *Nano Energy* **2020**, *68*, 104299.

- [24] F. Pianezzi, P. Reinhard, A. Chirilă, B. Bissig, S. Nishiwaki, S. Buecheler, A. N. Tiwari, *Phys. Chem. Chem. Phys.* **2014**, *16*, 8843.
- [25] B. Vermang, F. Rostvall, V. Fjällström, M. Edoff, *physica status solidi (RRL) – Rapid Research Letters* **2014**, *8*, 908.
- [26] D. Rudmann, D. Brémaud, H. Zogg, A. N. Tiwari, *Journal of Applied Physics* **2005**, *97*, 084903.
- [27] J. Lindahl, J. Keller, O. Donzel-Gargand, P. Szaniawski, M. Edoff, T. Törndahl, *Solar Energy Materials and Solar Cells* **2016**, *144*, 684.
- [28] J. Keller, F. Chalvet, J. Joel, A. Aijaz, T. Kubart, L. Riekehr, M. Edoff, L. Stolt, T. Törndahl, *Progress in Photovoltaics: Research and Applications* **2018**, *26*, 13.
- [29] A. Laemmle, R. Wuerz, M. Powalla, *Thin Solid Films* **2015**, *582*, 27.
- [30] A. Villanueva-Tovar, T. Kodalle, C. A. Kaufmann, R. Schlatmann, R. Klenk, *Solar RRL* **2020**, *4*, 1900560.
- [31] T. Lepetit, S. Harel, L. Arzel, G. Ouyard, N. Barreau, *Progress in Photovoltaics: Research and Applications* **2017**, *25*, 1068.
- [32] T. Kodalle, T. Bertram, R. Schlatmann, C. A. Kaufmann, *IEEE Journal of Photovoltaics* **2019**, *9*, 1839.
- [33] M. Burgelman, P. Nollet, S. Degrave, *Thin Solid Films* **2000**, *361–362*, 527.
- [34] T. Kohl, N. A. Rivas, J. de Wild, D. G. Buldu, G. Birant, G. Brammertz, M. Meuris, F. U. Renner, J. Poortmans, B. Vermang, *ACS Appl. Energy Mater.* **2020**, *3*, 5120.
- [35] J. de Wild, D. G. Buldu, T. Kohl, G. Birant, G. Brammertz, M. Meuris, J. Poortmans, B. Vermang, *Journal of Applied Physics* **2020**, *128*, 163102.
- [36] D. Abou-Ras, N. Schäfer, C. J. Hages, S. Levchenko, J. Márquez, T. Unold, *Solar RRL* **2018**, *2*, 1700199.
- [37] M. Raghuvanshi, A. Vilalta-Clemente, C. Castro, S. Duguay, E. Cadel, P. Jackson, D. Hariskos, W. Witte, P. Pareige, *Nano Energy* **2019**, *60*, 103.
- [38] P. Schöppe, S. Schönherr, P. Jackson, R. Wuerz, W. Wisniewski, M. Ritzer, M. Zapf, A. Johannes, C. S. Schnohr, C. Ronning, *ACS Appl. Mater. Interfaces* **2018**, *10*, 40592.
- [39] Y. Sun, S. Lin, W. Li, S. Cheng, Y. Zhang, Y. Liu, W. Liu, *Engineering* **2017**, *3*, 452.
- [40] V. V. Afanas'ev, A. Stesmans, B. J. Mrstik, C. Zhao, *Appl. Phys. Lett.* **2002**, *81*, 1678.
- [41] T. V. Perevalov, V. A. Gritsenko, V. V. Kaichev, *The European Physical Journal - Applied Physics* **2010**, *52*.
- [42] V. R. Deline, W. Katz, C. A. Evans, P. Williams, *Appl. Phys. Lett.* **1978**, *33*, 832.
- [43] R. Wuerz, W. Hempel, P. Jackson, *Journal of Applied Physics* **2018**, *124*, 165305.
- [44] C.-W. Chen, H.-W. Tsai, Y.-C. Wang, Y.-C. Shih, T.-Y. Su, C.-H. Yang, W.-S. Lin, C.-H. Shen, J.-M. Shieh, Y.-L. Chueh, *Advanced Functional Materials* **2019**, *29*, 1905040.
- [45] D. Colombara, F. Werner, T. Schwarz, I. Cañero Infante, Y. Fleming, N. Valle, C. Spindler, E. Vacchieri, G. Rey, M. Guennou, M. Bouttemy, A. G. Manjón, I. Peral Alonso, M. Melchiorre, B. El Adib, B. Gault, D. Raabe, P. J. Dale, S. Siebentritt, *Nature Communications* **2018**, *9*, 826.
- [46] D. Colombara, K. Conley, M. Malitckaya, H.-P. Komsa, M. J. Puska, *J. Mater. Chem. A* **2020**, *8*, 6471.
- [47] H. Rodriguez-Alvarez, R. Mainz, S. Sadewasser, *Journal of Applied Physics* **2014**, *115*, 204913.
- [48] A. Chirilă, P. Reinhard, F. Pianezzi, P. Bloesch, A. R. Uhl, C. Fella, L. Kranz, D. Keller, C. Gretener, H. Hagendorfer, D. Jaeger, R. Erni, S. Nishiwaki, S. Buecheler, A. N. Tiwari, *Nature Materials* **2013**, *12*, 1107.
- [49] M. Malitckaya, H.-P. Komsa, V. Havu, M. J. Puska, *J. Phys. Chem. C* **2017**, *121*, 15516.
- [50] Z.-K. Yuan, S. Chen, Y. Xie, J.-S. Park, H. Xiang, X.-G. Gong, S.-H. Wei, *Advanced Energy Materials* **2016**, *6*, 1601191.
- [51] S. Lany, A. Zunger, *Journal of Applied Physics* **2006**, *100*, 113725.

- [52] M. Gloeckler, C. R. Jenkins, J. R. Sites, *MRS Online Proceedings Library* **2002**, 763, 522.
- [53] A. Niemegeers, M. Burgelman, R. Herberholz, U. Rau, D. Hariskos, H.-W. Schock, *Progress in Photovoltaics: Research and Applications* **1998**, 6, 407.
- [54] J. L. Gray, In *Handbook of Photovoltaic Science and Engineering*, John Wiley & Sons, Ltd, **2003**, pp. 61–112.